BiC-ODE: Bidirectionally Coupled Neural ODEs for Rapid Laminar Surface Reconstruction of the Human Cortex from 5T MRI

Shui Cao[1†], Lin Teng[1†], Lu Shi[2†], Zifeng Lian[1], Jiameng Liu[1], Feng Shi[3], Kaicong Sun[1], Xiangshui Meng[4(✉)], and Dinggang Shen[1,3,5(✉)]

[1] School of Biomedical Engineering & State Key Laboratory of Advanced Medical Materials and Devices, ShanghaiTech University, Shanghai 201210, China
[2] Department of Radiology, Qilu Hospital, Cheeloo College of Medicine, Shandong University, Jinan, China
[3] Department of Research and Development, United Imaging Intelligence, Shanghai 200230, China
[4] Department of Radiology, Qilu Hospital (Qingdao), Cheeloo College of Medicine, Shandong University, Qingdao, China
[5] Shanghai Clinical Research and Trial Center, Shanghai 201210, China
xiangshuimeng@163.com, Dinggang.Shen@gmail.com

Abstract. T2-weighted FLAIR MRI at 5T reveals cortical laminar patterns via a distinct hypointense band, offering enhanced contrast over 3T and greater clinical feasibility than 7T. Accurate whole-brain reconstruction of this band is crucial for analyzing signal-defined intracortical laminar morphology but faces a trade-off: optimization-based methods achieve high fidelity yet are computationally prohibitive, while deep learning methods are fast but are typically designed only to reconstruct white matter and pial surfaces. Here, we propose BiC-ODE (Bidirectionally Coupled Neural ODEs), the first unified deep learning framework to achieve fast and accurate surface reconstruction of the intracortical hypointense band from 5T MR images, bridging the gap between high-resolution intracortical-band surface reconstruction and clinical feasibility. Our core idea is to jointly deform the white matter surface outward and the pial surface inward, until they align with the inner and outer boundaries of the intracortical hypointense band in 5T FLAIR images, respectively. Extensive experiments demonstrate that BiC-ODE: (1) achieves high reconstruction fidelity by precisely aligning with the intracortical hypointense band, fully leveraging the enhanced laminar contrast and clinical accessibility of 5T MRI; (2) delivers rapid inference speed, enabling efficient processing of large-scale datasets; and (3) promotes consistent multi-surface modeling through a bidirectional coupling strategy, reducing ordering violations among the nested surfaces. Thus, our framework enables reliable analysis of signal-defined intracortical morphology across large-scale 5T cohorts. Our code is publicly available at `https://github.com/shuicao-water/BiC-ODE-code`.

Keywords: Hypointense band · 5T MRI · Surface reconstruction.

† Equal contribution.

1 Introduction

Cortical abnormalities can manifest as layer-selective injury or intracortical redistribution rather than uniform global atrophy [1,2,3,4,5,6]. The complex laminar organization of the human cerebral cortex can appear on MRI as distinct signal bands, notably the intracortical hypointense band [7]. However, visualizing this band presents a trade-off: standard 3T MRI lacks sufficient contrast beyond primary regions [8], while 7T MRI, though high-resolution, remains too costly for routine deployment [9]. Emerging 5T MRI offers a practical compromise, delivering 7T-comparable contrast with greater clinical feasibility. Recent studies confirm that intracortical hypointense bands are visible on 5T T2-weighted FLAIR images [10]. Accurate whole-brain surface reconstruction of this hypointense band is essential to unlock 5T MRI's potential for studying signal-defined intracortical laminar morphology.

Existing surface reconstruction methods face critical challenges when applied to the intracortical hypointense band. Optimization-based methods [10,11,12,13] achieve high fidelity by iteratively deforming surfaces using task-specific energy functions, yet their computational cost renders them impractical for large-scale analysis. Deep learning-based methods have substantially accelerated cortical surface reconstruction [14,15,16,17,18,19]. However, these methods have primarily been developed and evaluated for reconstructing conventional white matter (WM) and pial surfaces, rather than the surfaces of the intracortical hypointense bands. Although their architectures could potentially be adapted to this task, reconstructing the hypointense-band surfaces from 5T FLAIR requires supervision and image-driven constraints tailored to the band's signal contrast and relative position within the cortical ribbon. The present task also requires maintaining the anatomical ordering of the four nested surfaces: the WM surface, the inner and outer surfaces of the hypointense band, and the pial surface. This anatomical constraint motivates a bidirectional formulation in which the WM and pial surfaces are deformed from opposite directions toward the hypointense band boundaries while accounting for their relative position. Accordingly, an effective framework for this task should: (1) support efficient processing of large-scale cohorts; (2) accurately delineate the hypointense-band boundaries from 5T FLAIR images; and (3) preserve the anatomically expected ordering of the four nested surfaces.

To meet these challenges, we propose **BiC-ODE**, the first deep learning framework specifically designed for hypointense-band surface reconstruction from 5T FLAIR images: (1) Efficient Inference: By implementing deformation via Neural Ordinary Differential Equations (ODEs), our method operates without iterative optimization, functioning as an end-to-end framework that directly outputs the target surfaces. (2) Dual-Strategy Accuracy Assurance for Hypointense Band: We combine high-fidelity supervision using optimization-generated surfaces with three task-specific losses explicitly tailored to the unique contrast and structure of the hypointense band in 5T FLAIR images. (3) Bidirectionally Coupled Deformation for Multi-Surface Modeling: BiC-ODE jointly deforms the WM surface outward and pial surface inward via bidirectionally coupled Neural

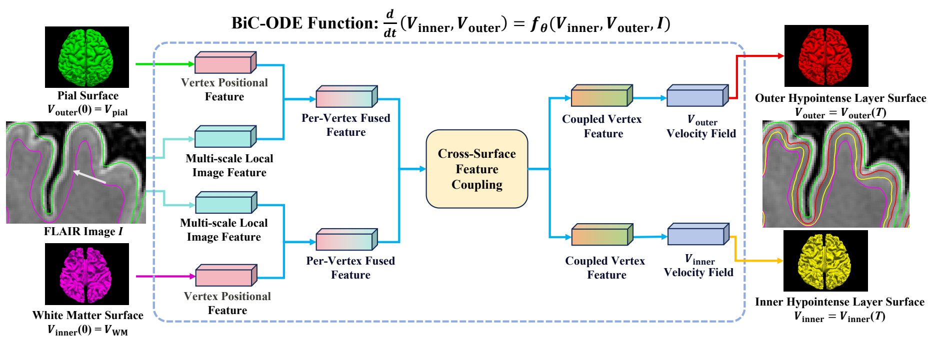

Fig. 1. Overview of the proposed BiC-ODE framework. Given a 5T FLAIR image as context, along with WM and pial surfaces as inputs, the Neural ODE network f_θ jointly deforms both cortical surfaces toward the boundaries of the hypointense band. The white arrow indicates the hypointense band in the image.

ODEs to align with the hypointense band boundaries. This encourages consistent relative positioning and reduces ordering violations among the nested surfaces.

Evaluated on 270 subjects with 5T MR images, BiC-ODE effectively addresses these challenges. Our method delivers efficient inference in seconds, enabling large-scale cohort processing. It achieves sub-millimeter accuracy comparable to optimization-generated ground truth, successfully capturing the unique laminar contrast of the hypointense band in 5T FLAIR images. To quantify the accuracy of the nested order among the four surfaces, we introduce the Surface Ordering Violation Rate (SOVR). Experiments show that our bidirectionally coupled formulation reduces SOVR and improves the consistency of nested surface ordering. In summary, BiC-ODE represents the first deep learning framework for hypointense-band surface reconstruction, enabling fast, accurate, and anatomically consistent large-scale laminar analysis with 5T MRI.

2 Method

2.1 Overview

Taking a 5T FLAIR image and a pair of WM and pial surfaces as input, our method reconstructs the inner and outer surfaces of the hypointense band via the **BiC-ODE** network (Fig. 1). This differentiable vector field f_θ predicts deformation velocities through three stages: (1) Multi-Source Feature Fusion: Per-vertex features are learned by fusing geometric positional encodings with multi-scale image contexts. (2) Cross-Surface Coupling: Features from both surfaces are integrated to augment each representation with its counterpart's state, providing bidirectional information sharing for consistent deformation. (3) Coupled Velocity Decoding: Coupled features are decoded into 3D velocity vectors to drive deformations of both cortical surfaces via Neural ODE integration, eventually converging onto the band boundaries.

2.2 Bidirectionally Coupled Neural ODEs

Our framework performs bidirectionally coupled deformation for multi-surface modeling, jointly deforming the WM and pial surfaces under shared Neural ODE dynamics. This serves two purposes: (1) preserving the nested order among the four surfaces, and (2) leveraging inter-surface spatial relationships to enhance reconstruction accuracy.

Formally, let $V_{\text{inner}}(t)$ and $V_{\text{outer}}(t) \in \mathbb{R}^{N\times 3}$ denote the vertex coordinates of the inner and outer surfaces of the hypointense band at time t, respectively. They are initialized as $V_{\text{inner}}(0) = V_{\text{WM}}$ and $V_{\text{outer}}(0) = V_{\text{pial}}$, where V_{WM} and $V_{\text{pial}} \in \mathbb{R}^{N\times 3}$ are the vertex sets of the WM and pial surfaces, respectively. Let I represent the input 5T FLAIR image. The joint dynamics of inner and outer surfaces are governed by the coupled ODE system:

$$\frac{d}{dt}(V_{\text{inner}}, V_{\text{outer}}) = f_\theta(V_{\text{inner}}, V_{\text{outer}}, I), \tag{1}$$

where the shared vector field f_θ conditions each surface's velocity on its own state, its counterpart, and image context. This continuous formulation enables efficient end-to-end inference via standard ODE solvers, eliminating iterative optimization. The final surfaces $V_{\text{inner}}(T)$ and $V_{\text{outer}}(T)$ are obtained by numerical integration over $t \in [0, T]$.

2.3 Network Architecture

As detailed in Fig. 1, BiC-ODE realizes the three stages through compact modules: (1) Multi-Source Feature Fusion: For each vertex, geometric features are encoded from 3D coordinates via a shared Multi-Layer Perceptron (MLP). Simultaneously, multi-scale local image features are captured by trilinearly sampling K^3 patches at three scales, aggregated via 3D convolutions, and projected by an MLP. These streams are concatenated and refined to form initial surface representations [14]. (2) Cross-Surface Coupling: To model inter-surface dependencies, we employ an asymmetric concatenation strategy where the feature order dictates the target surface: pial features precede WM features to generate the outer surface representation, whereas WM features lead for the inner surface. These ordered pairs are processed by a shared fusion network (with two MLP layers) to produce coupled features, conditioning each surface representation on its counterpart and encouraging consistent relative positioning during deformation. (3) Coupled Velocity Decoding: An output MLP decodes coupled features into 3D velocity vectors. These vectors define the vector field for a Neural ODE, numerically integrated by a standard solver to update vertex coordinates, driving the WM surface outward and the pial surface inward to converge on their respective target boundaries.

2.4 Learning Strategy

Our approach employs a dual strategy to ensure high-fidelity reconstruction of the hypointense band in 5T MR FLAIR images: silver-standard supervision from the optimization-based method [10], combined with task-specific deep learning constraints.

Silver-Standard Supervision. Our ground-truth surfaces of the hypointense band are derived from the optimization-based method [10] equipped with a task-specific energy function. This approach yields high-quality surfaces at 5T, serving as a rigorous silver standard to ensure the accuracy of our model.

Task-Specific Loss Functions. To further enhance reconstruction accuracy and enforce anatomical plausibility beyond simple supervision, we introduce three loss terms that act in concert:

(1) To ensure correct radial ordering of the predicted surfaces, we introduce the **depth consistency loss**, which penalizes deviations in normalized depth along WM-to-pial rays. For a vertex v_i, we define its normalized depth as $d(v_i) = \|v_i - v_{\text{WM},i}\|/(\|v_{\text{pial},i} - v_{\text{WM},i}\| + \epsilon)$ with $\epsilon = 10^{-8}$, and compute $\mathcal{L}_{\text{depth}} = \frac{1}{N}\sum_i \left(d(v_i^{\text{pred}}) - d(v_i^{\text{gt}})\right)^2$.

(2) To directly regularize the width of the hypointense band, we employ the **laminar thickness loss**, which enforces agreement between predicted and ground-truth inter-surface distances via $\mathcal{L}_{\text{thick}} = \frac{1}{N}\sum_i \left|\|v_{\text{outer},i}^{\text{pred}} - v_{\text{inner},i}^{\text{pred}}\| - \|v_{\text{outer},i}^{\text{gt}} - v_{\text{inner},i}^{\text{gt}}\|\right|$.

(3) To leverage the characteristic hypointensity of the target band, we introduce the **intensity band loss**. For each vertex pair $(v_{\text{inner},i}^{\text{pred}}, v_{\text{outer},i}^{\text{pred}})$, we uniformly sample n_{sample} points along the line segment connecting them, trilinearly interpolate the FLAIR intensity $I(\cdot)$ at these locations, and minimize their average value: $\mathcal{L}_{\text{band}} = \frac{1}{N}\sum_{i=1}^{N}\frac{1}{n_{\text{sample}}}\sum_{k=0}^{n_{\text{sample}}-1} I\Big((1-t_k)v_{\text{inner},i}^{\text{pred}} + t_k v_{\text{outer},i}^{\text{pred}}\Big)$, where $t_k = k/(n_{\text{sample}} - 1)$. This encourages the predicted surfaces to tightly enclose a low-intensity region consistent with the observed hypointense band. The mean squared error (MSE) and Laplacian smoothness losses $(\mathcal{L}_{\text{mse}}, \mathcal{L}_{\text{lap}})$ provide spatial accuracy and mesh regularity, respectively.

The total loss during training is formulated as:

$$\begin{aligned}\mathcal{L}_{\text{total}} = {} & \lambda_{\text{mse}}(\mathcal{L}_{\text{mse\_inner}} + \mathcal{L}_{\text{mse\_outer}}) + \lambda_{\text{depth}}(\mathcal{L}_{\text{depth\_inner}} + \mathcal{L}_{\text{depth\_outer}}) \\ & + \lambda_{\text{thick}}\mathcal{L}_{\text{thick}} + \lambda_{\text{band}}\mathcal{L}_{\text{band}} + \lambda_{\text{lap}}(\mathcal{L}_{\text{lap\_inner}} + \mathcal{L}_{\text{lap\_outer}}). \end{aligned} \tag{2}$$

where superscripts inner and outer indicate losses applied to the inner and outer surfaces of the hypointense band, respectively, and $\lambda_{\cdot}$ are balancing hyperparameters.

3 Experiments

3.1 Dataset and Preprocessing

The dataset contains 270 healthy subjects from a collaborating hospital (mean age: 54.4±14.5 years; 146 males) scanned with high-resolution 3D T1w sequences and T2w FLAIR sequences on a 5T scanner (uMR Jupiter, United Imaging Healthcare)[10]. This represents one of the largest 5T MRI datasets for laminar analysis to date. The cohort was randomly partitioned into 187 training, 41 validation, and 42 test subjects with no overlap. Data preprocessing was performed in two steps: (1) T1w and T2w FLAIR images were rigidly registered to the 24-month template of the UNC-BCP 4D brain atlas [20] with a resampled isotropic voxel size of 0.533 mm (385 × 457 × 318); and (2) the registered T1w images were processed with FreeSurfer[21] to generate the WM and pial cortical surfaces. The two resulting cortical surfaces together with the registered T2w FLAIR images served as the input to our model.

3.2 Implementation Details

Our model was implemented in PyTorch on a single NVIDIA A100 GPU. We integrated the ODE system using the Euler solver with a fixed step size of 0.1 and set $T = 1.0$. Training used the Adam optimizer with learning rate 1×10^{-4}. The model was trained for 500 epochs, taking approximately 100 hours to converge. Loss weights were set as $\lambda_{\text{mse}} = 1000$, $\lambda_{\text{depth}} = 0.01$, $\lambda_{\text{thick}} = 1$, $\lambda_{\text{band}} = 0.001$, and $\lambda_{\text{lap}} = 1$.

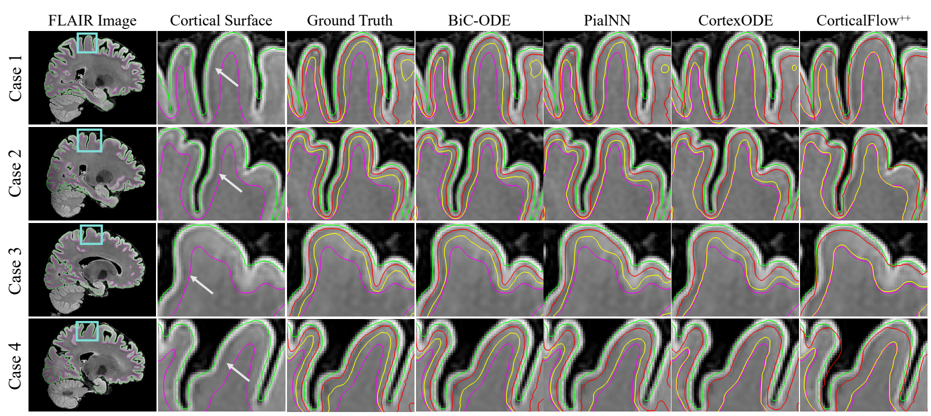

Fig. 2. Qualitative comparison of hypointense-band surface reconstructions across four cases using different methods. The purple, yellow, red, and green curves represent the WM, inner and outer surfaces of the hypointense band and the pial surface, respectively. The white arrow indicates the hypointense band in the images.

3.3 Evaluation Metrics

To assess reconstruction accuracy, we employ the Average Symmetric Surface Distance (ASSD) and the 90th percentile Hausdorff Distance (HD_{90}), both measured in millimeters. To evaluate structural integrity, we measure self-intersection artifacts using the Surface Intersection Fraction (SIF). Furthermore, to quantify the accuracy of the nested order among the four surfaces, we introduce the Surface Ordering Violation Rate (SOVR). SOVR quantifies the percentage of vertices that violate the expected radial cortical ordering from WM to pial across the four surfaces: the WM surface, the inner and outer surfaces of the hypointense band, and the pial surface. Specifically, for each vertex i, given the WM vertex $v_{\mathrm{WM},i}$ and pial vertex $v_{\mathrm{pial},i}$, we define the local column direction as $\hat{\mathbf{d}}_i = (v_{\mathrm{pial},i} - v_{\mathrm{WM},i})/(\|v_{\mathrm{pial},i} - v_{\mathrm{WM},i}\| + 10^{-8})$ and compute the scalar depth of any point v_i by projection $s(v_i) = (v_i - v_{\mathrm{WM},i})^\top \hat{\mathbf{d}}_i$. This yields $s_{\mathrm{WM},i} = 0$, $s_{\mathrm{inner},i} = s(v^{\mathrm{pred}}_{\mathrm{inner},i})$, $s_{\mathrm{outer},i} = s(v^{\mathrm{pred}}_{\mathrm{outer},i})$, and $s_{\mathrm{pial},i} = \|v_{\mathrm{pial},i} - v_{\mathrm{WM},i}\|$. A vertex is anatomically valid if $s_{\mathrm{WM},i} \leq s_{\mathrm{inner},i} \leq s_{\mathrm{outer},i} \leq s_{\mathrm{pial},i}$ holds within a tolerance of 10^{-5} mm. SOVR is then defined as the fraction of violating vertices:

$$\mathrm{SOVR} = 1 - \frac{1}{N}\sum_{i=1}^{N} \mathbb{I}\big(s_{\mathrm{WM},i} \leq s_{\mathrm{inner},i} \leq s_{\mathrm{outer},i} \leq s_{\mathrm{pial},i}\big), \tag{3}$$

where $\mathbb{I}(\cdot)$ denotes the indicator function.

3.4 Comparison with Deep Learning Methods

We compare our method against three leading deep learning-based surface reconstruction approaches: CortexODE [14], CorticalFlow^{++} [15], and PialNN [16]. Since these baselines target single-surface generation, we adapt them by using the WM and pial surfaces to predict the inner and outer surfaces of the hypointense band, respectively.

Table 1. Quantitative comparison of inner and outer surfaces of the hypointense band across different methods in terms of ASSD (mm), HD_{90} (mm), SIF (%), and SOVR (%), respectively.

Method	ASSD (mm)↓		HD_{90} (mm)↓		SIF (%)↓		SOVR (%)↓	
	Inner	Outer	Inner	Outer	Inner	Outer	Inner	Outer
Left								
Ours	**0.128 ± 0.014**	**0.142 ± 0.024**	**0.287 ± 0.036**	**0.306 ± 0.053**	0.005 ± 0.005	0.005 ± 0.005	**2.692 ± 0.386**	**2.692 ± 0.386**
CortexODE	0.268 ± 0.033	0.470 ± 0.107	0.656 ± 0.114	1.133 ± 0.237	0.006 ± 0.010	11.137 ± 3.367	11.847 ± 2.723	11.847 ± 2.723
CorticalFlow^{++}	0.637 ± 0.047	1.001 ± 0.058	1.297 ± 0.137	1.958 ± 0.139	**0.002 ± 0.004**	**0.002 ± 0.004**	38.020 ± 0.466	38.020 ± 0.466
PialNN	0.273 ± 0.018	0.316 ± 0.045	0.593 ± 0.057	0.688 ± 0.106	0.044 ± 0.042	2.897 ± 0.388	10.072 ± 2.460	10.072 ± 2.460
Right								
Ours	**0.138 ± 0.017**	**0.157 ± 0.031**	**0.308 ± 0.046**	**0.339 ± 0.066**	0.003 ± 0.003	0.003 ± 0.003	**2.358 ± 0.343**	**2.358 ± 0.343**
CortexODE	0.278 ± 0.035	0.474 ± 0.109	0.718 ± 0.119	1.138 ± 0.235	0.006 ± 0.010	10.505 ± 3.107	12.477 ± 3.285	12.477 ± 3.285
CorticalFlow^{++}	0.654 ± 0.049	1.066 ± 0.066	1.335 ± 0.145	2.126 ± 0.131	**0.002 ± 0.004**	**0.002 ± 0.004**	37.079 ± 0.923	37.079 ± 0.923
PialNN	0.275 ± 0.027	0.331 ± 0.049	0.642 ± 0.099	0.717 ± 0.117	0.022 ± 0.021	3.006 ± 0.597	9.882 ± 2.500	9.882 ± 2.500

Quantitative results in Table 1 show that our method achieves the best performance across all metrics, lowest ASSD (below 0.16 mm) and HD_{90} (below 0.34 mm) for all four surface types. Our SOVR is approximately 2.5%, far lower than CortexODE (∼12%), PialNN (∼10%), and CorticalFlow^{++} (∼37%), indicating that over 97% of predicted vertices respect the correct nested order. Although CorticalFlow^{++} achieves slightly lower SIF, its extremely high SOVR reflects a fundamental failure to preserve cortical topology. Qualitative results in Fig. 2 further support these findings. Our reconstructions match the accuracy of the optimization-based method while preserving the nested order among all four surfaces from WM to pial surfaces.

3.5 Ablation Study

We conduct an ablation study to assess the individual contributions of each loss term: depth consistency, laminar thickness, and intensity band losses, by systematically removing one from our full model. All variants use the same network architecture and differ only in the loss formulation.

As shown in Table 2, removing any loss term degrades performance, confirming their complementary roles. (1) Ablating the depth consistency loss consistently increases geometric error (ASSD increases by 0.04–0.07 mm, and HD_{90} increases by 0.09–0.14 mm) with little change in SIF or SOVR, highlighting its role in enforcing accurate radial positioning. (2) Removing the laminar thickness loss impairs inter-surface coherence, leading to higher SOVR (*e.g.*, increasing from 2.36% to 3.91% on the right hemisphere) and elevated HD_{90} and ASSD, which underscores the importance of enforcing consistent laminar spacing. (3) Finally, ablating the intensity band loss causes the most pronounced degradation in geometric accuracy: ASSD increases by 0.05–0.08 mm and HD_{90} by 0.12–0.17 mm, while SOVR rises by up to 1.3%. This demonstrates that image-driven guidance from the FLAIR hypointense band is essential for aligning reconstructed surfaces with intensity evidence.

Table 2. Ablation analysis of depth consistency, laminar thickness, and intensity band losses for inner and outer surfaces of the hypointense band in terms of ASSD (mm), HD_{90} (mm), SIF (%), and SOVR (%), respectively.

Variant	ASSD (mm)↓		HD_{90} (mm)↓		SIF (%)↓		SOVR (%)↓	
	Inner	Outer	Inner	Outer	Inner	Outer	Inner	Outer
Left								
Full model	**0.128 ± 0.014**	**0.142 ± 0.024**	**0.287 ± 0.036**	**0.306 ± 0.053**	0.005 ± 0.005	0.005 ± 0.005	2.692 ± 0.386	2.692 ± 0.386
w/o depth loss	0.192 ± 0.026	0.207 ± 0.035	0.422 ± 0.064	0.451 ± 0.076	0.005 ± 0.006	0.004 ± 0.006	**2.530 ± 0.377**	**2.530 ± 0.377**
w/o thickness loss	0.181 ± 0.025	0.197 ± 0.034	0.395 ± 0.061	0.425 ± 0.075	0.005 ± 0.005	**0.004 ± 0.004**	2.578 ± 0.449	2.578 ± 0.449
w/o band loss	0.193 ± 0.023	0.219 ± 0.036	0.422 ± 0.057	0.471 ± 0.071	**0.004 ± 0.004**	**0.004 ± 0.004**	4.023 ± 0.571	4.023 ± 0.571
Right								
Full model	**0.138 ± 0.017**	**0.157 ± 0.031**	**0.308 ± 0.046**	**0.339 ± 0.066**	**0.003 ± 0.003**	**0.003 ± 0.003**	2.358 ± 0.343	2.358 ± 0.343
w/o depth loss	0.185 ± 0.031	0.196 ± 0.040	0.402 ± 0.072	0.425 ± 0.086	0.004 ± 0.004	0.003 ± 0.004	**2.012 ± 0.448**	**2.012 ± 0.448**
w/o thickness loss	0.199 ± 0.023	0.209 ± 0.037	0.446 ± 0.063	0.452 ± 0.077	0.004 ± 0.004	0.004 ± 0.006	3.911 ± 0.427	3.911 ± 0.427
w/o band loss	0.195 ± 0.036	0.210 ± 0.037	0.426 ± 0.080	0.452 ± 0.079	0.004 ± 0.004	0.003 ± 0.004	3.323 ± 0.583	3.323 ± 0.583

3.6 Computational Efficiency

For surface reconstruction of the hypointense band, our method requires only 3.47 seconds per subject, outperforming PialNN (6.95 s), CorticalFlow^{++} (9.54 s), and CortexODE (12.07 s). Most importantly, compared to the optimization-based method used for generating GT surfaces ($\sim$2.5 hours), our method reduces inference time to seconds, making it feasible for large-scale cohort studies.

4 Conclusion

In this study, we have presented a novel deep learning framework to reconstruct the inner and outer surfaces of the intracortical hypointense band from 5T MR images via a bidirectionally coupled Neural ODE system. Extensive validation on a dataset of 270 subjects with 5T MRI demonstrates that our approach matches the sub-millimeter precision of optimization-based methods while leveraging the efficiency of deep learning to accelerate inference from hours to seconds. This work fully leverages both the enhanced laminar contrast and clinical accessibility of 5T MRI, thereby unlocking its potential for large-scale cortical laminar microstructure analysis.

Acknowledgments. This work was supported in part by National Natural Science Foundation of China (grant numbers 62131015, U23A20295, 82441023, 82394432), the China Ministry of Science and Technology (grant numbers STI2030-Major Projects-2022ZD0209000, STI2030-Major Projects-2022ZD0213100), the Key R&D Program of Guangdong Province, China (grant number 2023B0303040001), HPC Platform of ShanghaiTech University, and Qingdao Science and Technology for People's Livelihood Demonstration Special Project (grant number 26-1-5-smjk-15-nsh).

Disclosure of Interests. All authors declare no conflicts of interest.

References

1. Till S Zimmer, Adam L Orr, and Anna G Orr. Astrocytes in selective vulnerability to neurodegenerative disease. *Trends in neurosciences*, 47(4):289–302, 2024.
2. Masoud Etemadifar, Kamran Rezaei, Fatemeh Hojjati Pour, and Mehri Salari. Subpial cortical demyelination in multiple sclerosis: A systematic review of frequency, pathology, and clinical diversity. *Multiple Sclerosis and Related Disorders*, 101:106569, 2025.
3. Roland Coras, Hans Holthausen, and Harvey B Sarnat. Focal cortical dysplasia type 1. *Brain pathology*, 31(4):e12964, 2021.
4. Hannah Spitzer, Mathilde Ripart, Kirstie Whitaker, Felice D'Arco, Kshitij Mankad, Andrew A Chen, Antonio Napolitano, Luca De Palma, Alessandro De Benedictis, Stephen Foldes, et al. Interpretable surface-based detection of focal cortical dysplasias: a multi-centre epilepsy lesion detection study. *Brain*, 145(11):3859–3871, 2022.
5. Yingfan Wang, Minghao Li, Huijun Li, Wei Yu, Peilin Jiang, Xinyi Zhou, Ke Hu, Feng Yang, Jiu Chen, Ming Yang, et al. Altered neurostructural development in magnetic resonance imaging-negative pediatric epilepsy: A large-scale multicenter study of 1919 children. *Epilepsia*, 67(4):1873–1886, 2026.
6. Richard A Armstrong. Cortical laminar distribution of β-amyloid deposits in five neurodegenerative disorders. *Folia Neuropathologica*, 58(1):1–9, 2020.
7. Robert Trampel, Pierre-Louis Bazin, Kerrin Pine, and Nikolaus Weiskopf. In-vivo magnetic resonance imaging (mri) of laminae in the human cortex. *NeuroImage*, 197:707–715, 2019.
8. Koji Kamada, Shingo Kakeda, Norihiro Ohnari, Junji Moriya, Toru Sato, and Yukunori Korogi. Signal intensity of motor and sensory cortices on t2-weighted and flair images: intraindividual comparison of 1.5 t and 3t mri. *European radiology*, 18(12):2949–2955, 2008.
9. Jaco JM Zwanenburg, Jeroen Hendrikse, and Peter R Luijten. Generalized multiple-layer appearance of the cerebral cortex with 3d flair 7.0-t mr imaging. *Radiology*, 262(3):995–1001, 2012.

10. Shui Cao, Lu Shi, Jiameng Liu, Zifeng Lian, Lin Teng, Qin Xiao, Xiaona Xia, Kaicong Sun, Feng Shi, Xiangshui Meng, and Dinggang Shen. In vivo surface reconstruction of three signal-defined intracortical layers using 5T 3D FLAIR MR imaging. *bioRxiv*, 2026.
11. Gang Li, Jingxin Nie, Guorong Wu, Yaping Wang, Dinggang Shen, Alzheimer's Disease Neuroimaging Initiative, et al. Consistent reconstruction of cortical surfaces from longitudinal brain mr images. *Neuroimage*, 59(4):3805–3820, 2012.
12. Tianming Liu, Jingxin Nie, Ashley Tarokh, Lei Guo, and Stephen TC Wong. Reconstruction of central cortical surface from brain mri images: method and application. *NeuroImage*, 40(3):991–1002, 2008.
13. Chenyang Xu, Dzung L Pham, Maryam E Rettmann, Daphne N. Yu, and Jerry L Prince. Reconstruction of the human cerebral cortex from magnetic resonance images. *IEEE Transactions on Medical Imaging*, 18(6):467–480, 2002.
14. Qiang Ma, Liu Li, Emma C. Robinson, Bernhard Kainz, Daniel Rueckert, and Amir Alansary. Cortexode: Learning cortical surface reconstruction by neural odes. *IEEE Transactions on Medical Imaging*, 42(2):430–443, 2023.
15. Rodrigo Santa Cruz, Léo Lebrat, Darren Fu, Pierrick Bourgeat, Jurgen Fripp, Clinton Fookes, and Olivier Salvado. Corticalflow^{++}: Boosting cortical surface reconstruction accuracy, regularity, and interoperability. In Linwei Wang, Qi Dou, P. Thomas Fletcher, Stefanie Speidel, and Shuo Li, editors, *Medical Image Computing and Computer Assisted Intervention – MICCAI 2022*, pages 496–505, Cham, 2022. Springer Nature Switzerland.
16. Qiang Ma, Emma C. Robinson, Bernhard Kainz, Daniel Rueckert, and Amir Alansary. Pialnn: A fast deep learning framework for cortical pial surface reconstruction. In Ahmed Abdulkadir, Seyed Mostafa Kia, Mohamad Habes, Vinod Kumar, Jane Maryam Rondina, Chantal Tax, and Thomas Wolfers, editors, *Machine Learning in Clinical Neuroimaging*, pages 73–81, Cham, 2021. Springer International Publishing.
17. Andrew Hoopes, Juan Eugenio Iglesias, Bruce Fischl, Douglas Greve, and Adrian V Dalca. Topofit: rapid reconstruction of topologically-correct cortical surfaces. *Proceedings of machine learning research*, 172:508, 2022.
18. Fabian Bongratz, Anne-Marie Rickmann, Sebastian Pölsterl, and Christian Wachinger. Vox2cortex: Fast explicit reconstruction of cortical surfaces from 3d mri scans with geometric deep neural networks. In *Proceedings of the IEEE/CVF conference on computer vision and pattern recognition*, pages 20773–20783, 2022.
19. Fabian Bongratz, Anne-Marie Rickmann, and Christian Wachinger. Neural deformation fields for template-based reconstruction of cortical surfaces from mri. *Medical Image Analysis*, 93:103093, 2024.
20. Liangjun Chen, Zhengwang Wu, Dan Hu, Ya Wang, Fenqiang Zhao, Tao Zhong, Weili Lin, Li Wang, and Gang Li. A 4d infant brain volumetric atlas based on the unc/umn baby connectome project (bcp) cohort. *NeuroImage*, 253:119097, 2022.
21. Bruce Fischl. Freesurfer. *NeuroImage*, 62(2):774–781, 2012. 20 YEARS OF fMRI.